



The impact of impervious surface, vegetation, and soil areas on land surface temperatures in a semi-arid region using Landsat satellite images enriched with Ndaisi method data

Mustafa Hayri Kesikoglu · Coskun Ozkan · Tolga Kaynak

Received: 26 June 2020 / Accepted: 26 January 2021 / Published online: 24 February 2021
© The Author(s), under exclusive licence to Springer Nature Switzerland AG part of Springer Nature 2021

Abstract Impervious surfaces are a significant issue of both urbanization and environmental assessment. However, it is a problem to classify impervious surface (IS) and soil areas as separate classes in land cover classification. The objectives of this study are to obtain impervious surface, vegetation, and soil areas clearly of an urban complex with a semi-arid climate and to better determine the relationships of IS, vegetation, and soil areas with land surface temperatures (LSTs). For this purpose, IS, vegetation, and soil areas in a semi-arid city of Turkey-Kayseri city were identified by using Normalized Difference Anthropogenic Impervious Surface Index (NDAISI) data and support vector machine (SVM) method together in the classification of different areas. Landsat 5, 7, and 8 satellite images of 1987, 2000, and 2013 were used, respectively, in this study. Afterward, the effects of these areas on LSTs were analyzed. Regression analysis was used to determine the relationships between land cover areas and surface temperatures. To better demonstrate these relationships, besides common pixel-based and

classical regional-based approaches, a new density-based regional analysis approach was proposed. This study is an innovative one in terms of detecting IS and indicating relationships between land cover areas and surface temperatures in semi-arid regions. Another innovation of the study is related to the results produced. The results showed that decreasing LST values were observed with increasing IS and vegetation cover values and increasing LST values were observed with increasing soil areas. The present findings may provide significant contributions to the literature and will facilitate the development of urban planning strategies in semi-arid regions.

Keywords Impervious surface · Land surface temperature · NDAISI · SVM · Landsat TM · ETM+ · OLI-TIRS · Kayseri

Introduction

According to the United Nations 2014 report, 54% of the world's population lives in urban areas and such a rate continues to grow and will reach 66% by the year 2050. This rate is estimated to be 73% in Turkey and is expected to reach 84% in 2050 (UNPD, 2015). Increasing populations, consequently increasing housing, work, and transportation areas and the rapid expansion of urban areas has become a constantly growing phenomenon. This growing phenomenon appears

M. H. Kesikoglu (✉)
Department of Geomatics Engineering, Usak University,
Usak, Turkey
e-mail: hayri.kesikoglu@usak.edu.tr; mkesikoglu@gmail.com

C. Ozkan · T. Kaynak
Department of Geomatics Engineering, Erciyes University,
Kayseri, Turkey

as the concept of urbanization (Kalnay & Cai, 2003). Urbanization causes rapid urban growth (Kaufmann et al., 2007). This situation concludes with changes in land use, regional ecosystem, and energy consumption due to anthropogenic influences such as buildings, construction zones, and roads with man-made features (Ma et al., 2012; Rashid & Romshoo, 2013; Guan et al., 2019). Also, these anthropogenic influences can have an impact on settled communities (Bhatti et al., 2019). One of the anthropogenic influences is impervious surfaces. Impervious surfaces are defined as surfaces such as roofs, sidewalks, roads, car parks, etc. consisting of areas built with waterproof materials such as asphalt, stone, and concrete. The amount of impervious surfaces is also one of the most important indicators of urbanization degree and environmental quality increase with the urbanization (Arnold & Gibbons, 1996; Paul & Meyer, 2001). The impact of urbanization on the environment is often understood by determining the interaction with impervious surfaces. Therefore, monitoring and mapping of impervious surfaces are very important in preparing adaptation strategies for regional climate and ecosystem changes (Bierwagen et al., 2010; Lyu et al., 2019). In addition to ground measurements, advanced geospatial techniques using GPS measurements, photogrammetry, and remote sensing images can be used to map the impervious surface area (ISA). The remote sensing method has advantages over the other methods such as the ability to map very large areas at low cost and in less time and integration with Geographic Information Systems (GIS) (Bauer et al., 2004).

There are many methods for estimating impervious surfaces based on spectral or geospatial information obtained from remote sensing images. When looking at these methods, different approaches can be listed as follows: (1) selecting areas to be classified manually or semi-automatically, and determining class labels as a result of visual interpretation (Jennings et al., 2004; Gluch et al., 2006); (2) evaluating data from the other data sources, such as vegetation and soil (VIS-Vegetation-Impervious Surface-Soil model) (Phinn et al., 2002; Okujeni et al., 2015); (3) using index values (Bauer et al., 2004; Yang & Liu, 2005; Wang et al., 2015b); (4) using spectral mixture analysis (SMA) (Phinn et al., 2002; Wu & Murray, 2003; Xian & Crane, 2005; Lu & Weng, 2006); (5) using

decision tree algorithm (Xian et al., 2008; Couturier et al., 2011).

Impervious surface areas (ISAs) are complex structures having similar reflectance with soil. It is a problem to classify impervious surface (IS) and soil areas as separate classes in land cover classification (Xu et al., 2013). When the studies are examined, it is seen that most of the produced approaches were tried in the tropic or sub-tropic regions (Zhang et al., 2009; Xu et al., 2013; Acero & González-Asensio, 2018; Govil et al., 2019; Sun et al., 2019). Besides, the relationships among ISA, vegetation, soil classes, and corresponding land surface temperatures (LSTs) are very limited in semi-arid regions (Çiçek et al., 2013; Haashemi et al., 2016). Therefore, this study has two major objectives. First, we aim to classify ISA in a semi-arid region which was not considered much in previous literature. This study is an innovative one in terms of performance of ISA analysis with the use of the support vector machine (SVM) classification method with the aid of Normalized Difference Anthropogenic Impervious Surface Index (NDAISI) data. The second objective is to analyze the effects of ISA, vegetation, and soil on LST in a semi-arid region with the development of a new density-based regional analysis approach. Therefore, this study will have a major contribution to the classification of the semi-arid region.

In this sense, ISA was determined for Kayseri province of Turkey and the relationships between ISA and LST were determined. Initially, Modified Normalized Difference Water Index (MNDWI) (Li et al., 2014) was used to determine the areas of water bodies (Esch et al., 2009). Then, NDAISI, a derivative index-based method, was used to calculate ISAs semi-automatically (Piyooosh & Ghosh, 2017). NDAISI operates over the outcomes obtained through different index methods and developed for Landsat 8 satellite data. Therefore, while using NDAISI, modifications were performed in some operational steps to develop a new approach as to be commonly used for all three of Landsat 5, 7, and 8 satellite images. With the aid of the methods used in this classification approach, the ranges in which resultant outcomes were intensified were taken into consideration and Otsu's binary thresholding method (OT) (Otsu, 1979) or manual data thresholding was performed to determine ISAs partially. Since index data are alone insufficient for ISA determination, they were added as supplementary

data to visible, infrared, and thermal region bands of the satellite image and original attribute space was enriched. This multi-mode attribute space was classified with the SVM method and ISA was determined. Then, after the radiometric calibration of thermal band data of geometrically registered Landsat 5, 7, and 8 satellite images to investigate the effects of ISA on LST, the surface temperatures of the land cover were obtained. Finally, simple linear regression analyses were performed to determine the relationships among ISA, vegetation, soil classes, and corresponding LSTs and statistical tests were used to test the significance of regression models.

The remainder of this study is organized as follows. The study area and data section comprise descriptive information about the data used and the general characteristics of the workspace. The methodology section includes a detailed methodology containing the classification approach used to find out ISAs with the aid of NDAISI data and SVM method, the

procedures for LST generation, and data preparation approach for statistical analyses including pixel-based and density-based zonal analysis. Outcomes of accuracy assessment for the classification approach and the relationship between ISA, Normalized Difference Vegetation Index (NDVI), soil, and LST are given and discussed in the results and discussion section. Finally, the paper is completed with concluding remarks and some implications in the conclusion section.

Study area and data

The city center including three central towns of Kayseri province was selected as the study area (Fig. 1).

Kayseri province is in the Central Anatolia Region of Turkey between 34°56'–36°59' east longitudes and 37° 45'–38° 18' north latitudes. It is a greater city municipality and according to 2016 statistics,

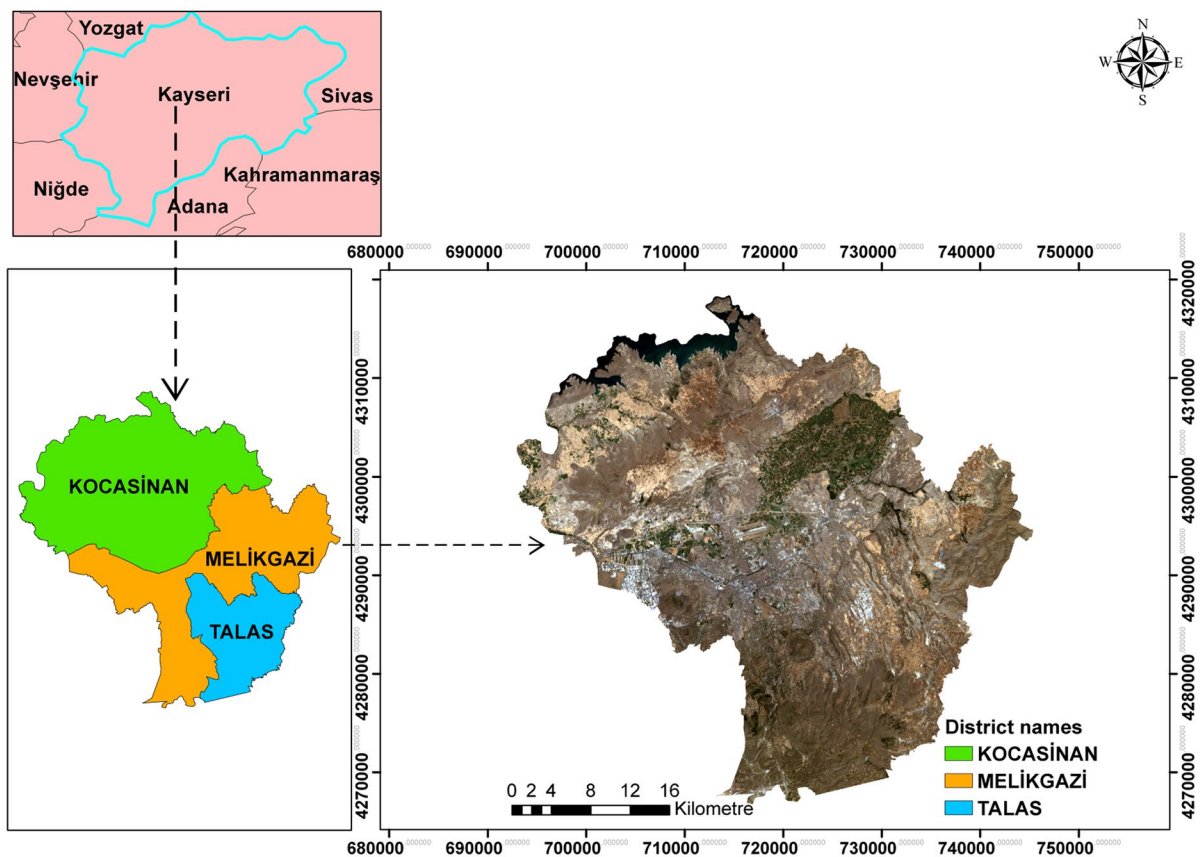
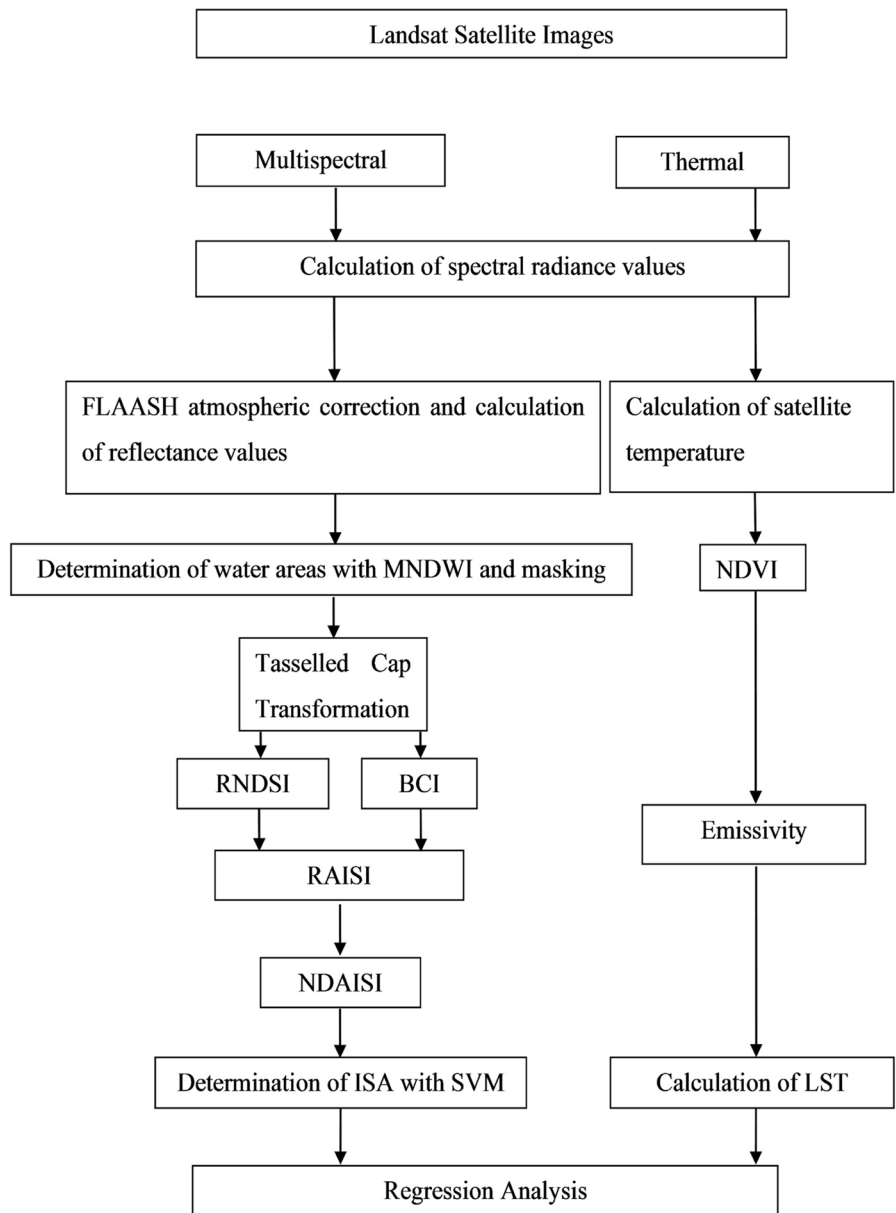


Fig. 1 Location map of Kayseri study area

Kayseri is the 14th most crowded city in Turkey. Kayseri has quite intensive industrial activities. The city is in a rapid urbanization process (Wikipedia, 2019). Kayseri has a semi-arid climate with hot and dry summers and cold and wet winters (Erinc, 1950). The greatest temperatures are observed in July and August. Steppe areas are dominant over the smooth terrains, mountainous, and hilly terrains. There is a sparse forest cover at high altitudes, but soils are mostly covered with destructed forest and shrub

covers. There are quite large barren soils in the study area. Just because of land cover diversity and rapid urbanization, this study area was selected for ISA determination and analysis of the relationships with land surface temperatures. For quantitative assessment of ISA and LST, Landsat 5 TM image taken on 20 July 1987, Landsat 7 ETM+ image taken on 31 July 2000, and Landsat 8 LDCM OLI/TIRS image taken on 11 July 2013 were used (Fig. 2). Satellite images were in Universal Transverse Mercator (UTM)

Fig. 2 Flowchart of the study



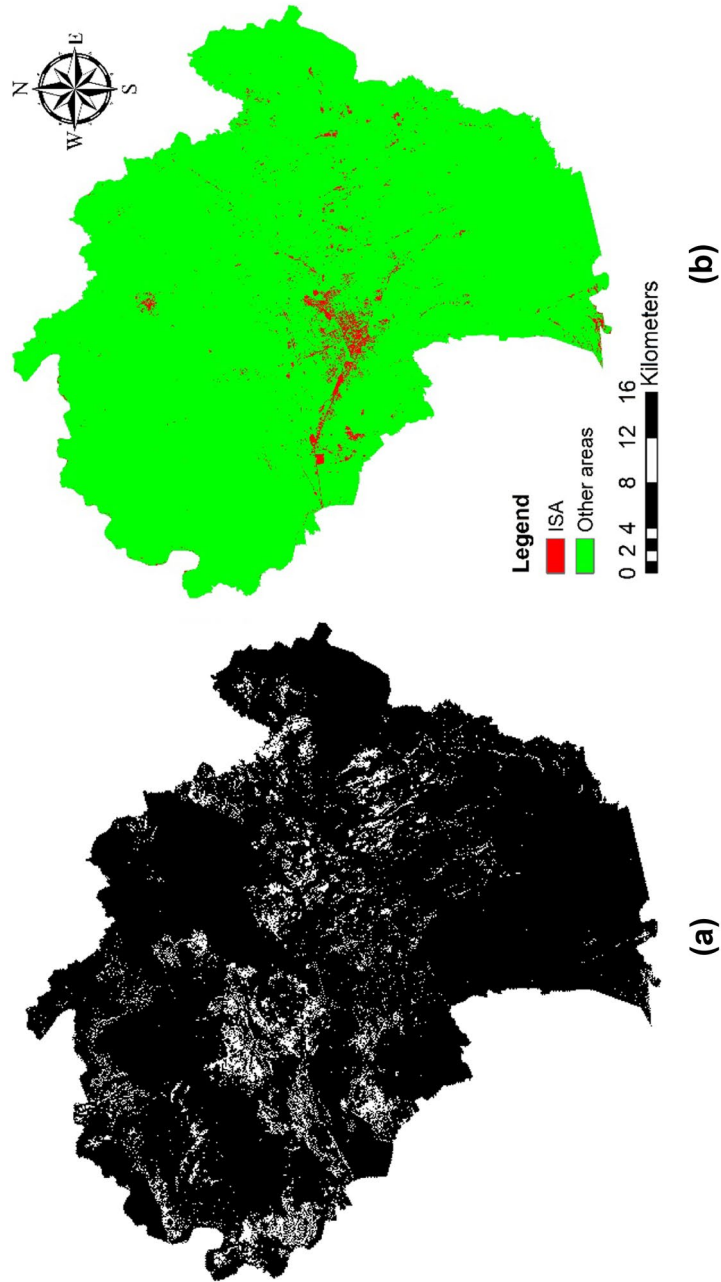


Fig. 3 **a** NDAISI, **b** classification images belonging to 1987

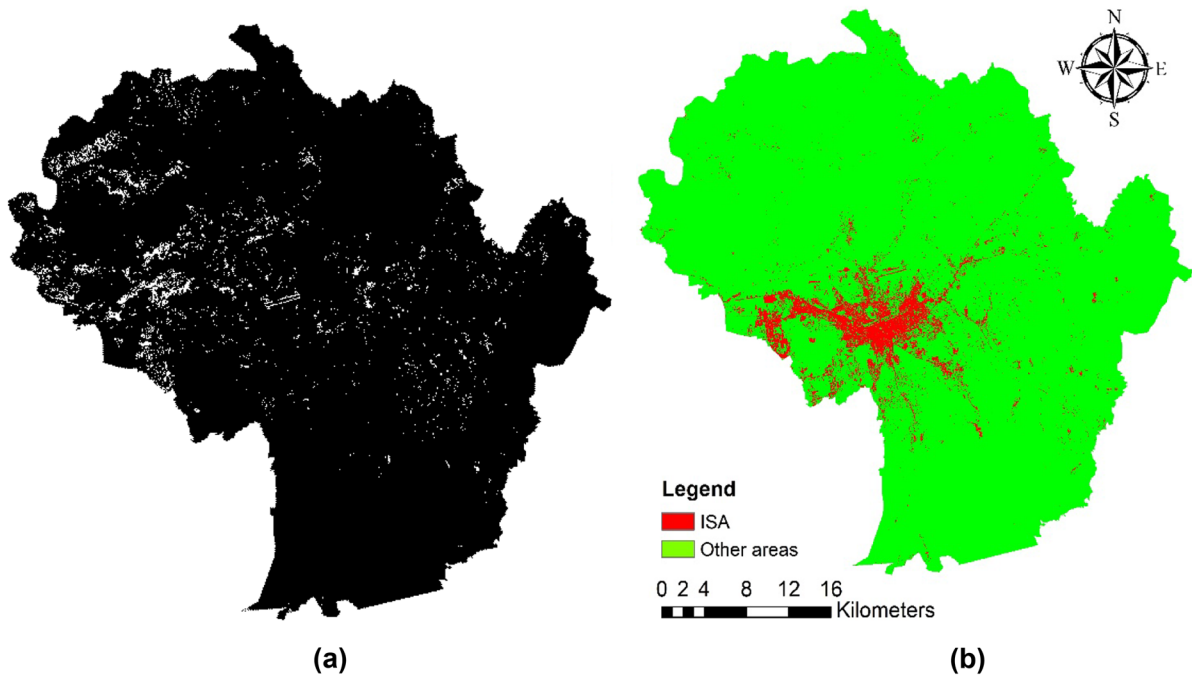


Fig. 4 a NDAISI, b classification images belonging to 2000

projection coordinate system and World Geodetic System 84 (WGS84) datum. Landsat 5 TM satellite image of 1987 was selected as a reference image to

study the borders of the same locations in Landsat 5, 7, and 8 satellite images belonging to different years, and image recording was carried out by resampling

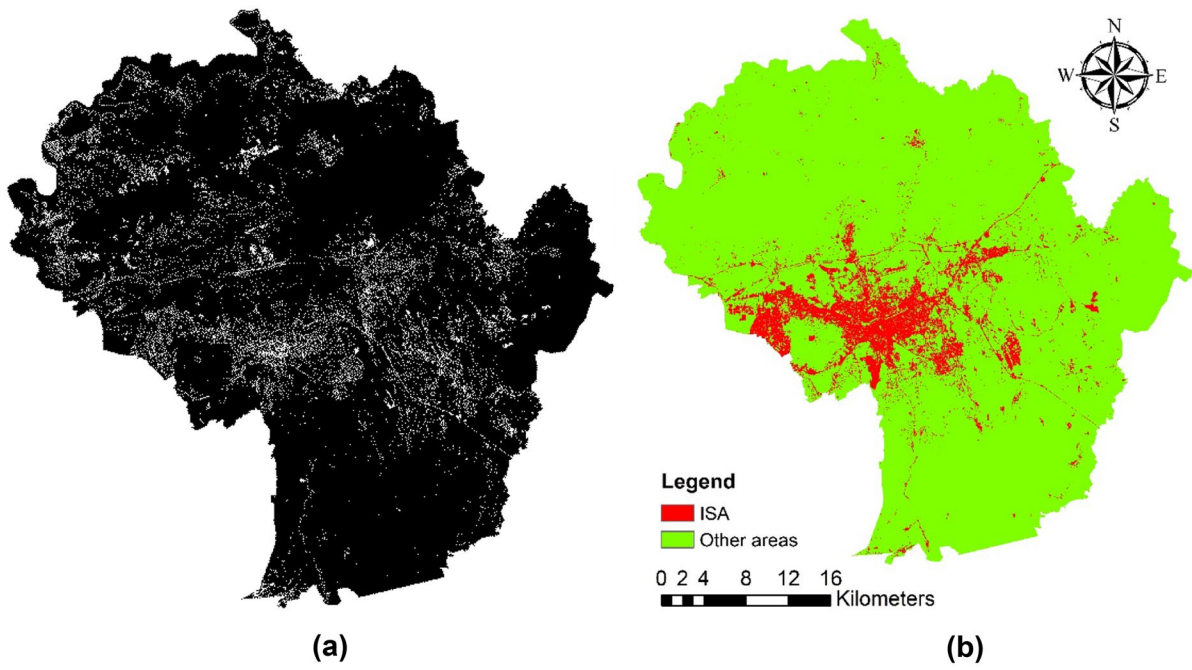


Fig. 5 a NDAISI, b classification images belonging to 2013

Table 1 ϵ values for Landsat 5, Landsat 7, and Landsat 8 satellites

NDVI thresholds	Landsat 5 and Landsat 7	Landsat 8
NDVI < 0.2	0.97	0.966
0.2 ≤ NDVI ≤ 0.5	0.004Pv + 0.986	1.0094 + 0.047ln(NDVI)
NDVI > 0.5	0.99	0.973

other multi-band images according to the reference image. Ground control points with an RMSE value below 0.5 pixels were used in the image resampling step. Therefore, geometrically registered images were obtained.

Methodology

Impervious surfaces

The classification approach used to find out ISAs with the aid of NDAISI (Piyooosh & Ghosh, 2017) and SVM (Kesikoglu et al., 2019) methods is presented in Fig. 2. Initially, spectral radiance calibration was performed by converting digital number (DN) values of Landsat satellite images into radiance values. Then, spectral radiance values were passed through FLAASH atmospheric correction with the aid of ENVI5.3 software to eliminate reflected energy radiance and dissipation-induced effects. In index-based methods, accuracy in the determination of ISAs decreases when the water areas were not identified (Xu, 2010). In the present study, the MNDWI method was used to determine water areas. Water areas were identified and masked through OT thresholding of Landsat 5, Landsat 7, and Landsat 8 index image data.

It is necessary to calculate the RAISI method to get the NDAISI method. In previous literature (Piyooosh & Ghosh, 2017), BCI (Deng & Wu, 2012) and Modified Normalized Difference Soil Index

(MNDSI) (Piyooosh & Ghosh, 2018) methods were used to get the RAISI method. MNDSI method uses panchromatic band data while making calculations. While Landsat 7 and Landsat 8 satellite images used in this study had panchromatic band data, Landsat 5 image did not. Therefore, instead of the MNDSI method allowing information retrieval to get the RAISI method and soil areas, Ratio Normalized Difference Soil Index (RNDSI) method was used to have the same methods in the identification of ISAs (Deng et al., 2015).

To get desired areas from the index images obtained through consecutive use of the above-mentioned methods, images should pass through thresholding. For threshold value, the OT method (Otsu, 1979; Li et al., 2013; Du et al., 2014) and manual thresholding approaches were used. The manual thresholding approach in the study is based on taking the median of the positive index values in the areas of the desired image class. At the end of thresholding, while ISAs were able to be distinguished in some soil areas, they were not clearly identified in some soil areas and some impervious surfaces were diagnosed as soil. When the entire study area was analyzed, it was observed that the use of the method alone was not able to distinguish ISAs sufficiently because of high quantities of soil areas (Figs. 3a, 4a, and 5a). Since index data were not sufficient alone for the identification of

Table 2 Classification accuracies of SVM with/without NDAISI

Method		1987	2000	2013
SVM without NDAISI	Overall accuracy (%)	88.57	91.79	94.07
	Kappa (%)	74.00	82.00	87.15
SVM with NDAISI	Overall accuracy (%)	90.30	92.09	94.87
	Kappa (%)	78.20	82.70	89.00

Table 3 Class-based accuracies of SVM with NDAISI for 1987, 2000, and 2013

	Class	Producer’s accuracy (%)	User’s accuracy (%)
1987	Impervious surface	74.1	100
	Other	100	86.6
2000	Impervious surface	82.54	94.89
	Other	97.33	90.28
2013	Impervious surface	90.77	95.33
	Other	97.33	94.62

ISAs, index image was supplemented into visible, infrared, and thermal region bands of satellite image as supplementary data, and ISAs were determined through the classification of satellite image with the aid of the SVM method (Kesikoğlu, 2013; Sahu et al., 2015). Data attribute space was enriched through additions of NDAISI method data into satellite image bands as supplementary data.

Land surface temperature

LST is determined with the aid of thermal band data of satellite images. Landsat 5 and Landsat 7 satellites have one thermal band. However, Landsat 8 has two thermal bands as Band 10 and Band 11. It is recommended that Band 10 should be preferred while findings of LST since calibration values are more reliable than Band 11 (USGS, 2018). In this study, the method developed by Chander and Markham (2003) able to make calculations without a need for any atmospheric parameters was used in the calculation of LST (Chander & Markham, 2003; Weng et al., 2004; Nichol, 2005; Estoque et al., 2017). Emissivity (ϵ) value, which varies according to land cover types, is used to obtain land surface temperatures. In this study, the emissivity values used to get LST were calculated by using NDVI thresholding method described in Table 1 (Sobrino et al., 2004; Zhang et al., 2009).

Soil ($\text{NDVI} < 0.2$) and vegetation ($\text{NDVI} > 0.5$) ϵ values for Landsat 5 TM and Landsat 7 ETM+ satellites were, respectively, taken as 0.97 and 0.99, ϵ values of mixed sections ($0.2 \leq \text{NDVI} \leq 0.5$) were calculated with the equation of $\epsilon = 0.004P_v + 0.986$ (Sobrino et al., 2004). Soil ($\text{NDVI} < 0.2$) and vegetation ($\text{NDVI} > 0.5$) ϵ values for Landsat 8 TIRS satellite were, respectively, taken as 0.966 and 0.973 (Wang et al., 2015a), ϵ values of mixed sections ($0.2 \leq \text{NDVI} \leq 0.5$) were calculated with the equation of $\epsilon = 1.0094 + 0.047 \ln(\text{NDVI})$ (Sekertekin et al., 2016). P_v refers to the vegetative ratio in Table 1. $\text{NDVI}_{\text{soil}}$ and $\text{NDVI}_{\text{vegetation}}$ can be described, respectively, as 0.2 and 0.5 given in Eq. 1.

$$P_v = \left(\frac{\text{NDVI} - \text{NDVI}_{\text{soil}}}{\text{NDVI}_{\text{vegetation}} - \text{NDVI}_{\text{soil}}} \right)^2 \quad (1)$$

Data preparation

Relationships are assessed in two fashions, either pixel-based or zonal-based. Two different assessment types are used for better visualization of the relationships. In some previous studies (Xu, 2010; Xu et al., 2013), it was observed that when the pixels were analyzed alone, they were able to present the relationships between ISA and LST strongly. In some other studies (Yuan & Bauer, 2007; Zhang et al., 2009; Li et al., 2011), on the other hand, it was indicated that when the pixels were analyzed alone, they were not able to set a quantitative relationship between ISA and LST or set a weak relationship. Such a case hampers the interpretation of the relationships between ISA and LST. The resultant weak assessment of the relationships between ISA and LST when the pixels were analyzed alone was attributed to the confusion of IS and soil area with each other during the classification (Xu et al., 2013). Thusly, in present classifications, IS and soil areas were not able to be distinguished in some places. In such cases, instead of single-pixel, zonal-based analyses may generate more efficient outcomes for the relationships between ISA-LST (Xu et al., 2013). Therefore, in this study, two different analysis approaches (pixel and density-based zonal) were employed in the presentation of the relationships between ISA and LST. In this way, outcomes of “Pixel-Based Analysis (PBA)” and “Density-Based Zonal Analysis (DBZA)” were able to be observed. In PBA, attribute space is divided into an equal interval based on the minimum and maximum values. Average input and output values of each interval are calculated and a regression graph is drawn (Lu & Weng, 2006; Yuan & Bauer, 2007). In DBZA, the density of data within $A \times A$ blocks is taken into consideration. Density is calculated as the ratio of the sum of membership values of pixels of input data (ISA, vegetation, or soil) to the sum of membership values of all pixels of the block. Then, the arithmetic mean of output (LST) values of all pixels is calculated. After that, the density values in 0–1 interval are divided into n number of sub-intervals. The average of LST values of the blocks with a density falling into the same interval is taken and the regression graph is drawn. Considering the spatial resolution of the satellite images, in DBZA approach, block size was taken as 3×3 and number of intervals was taken 35. Block size and number

of intervals were found to be sufficient at the end of works done on data of 3 years.

Results and discussion

Analysis of ISA

With the integrated use of NDAISI and SVM methods, an efficient classification approach was presented for ISAs. When the ISAs obtained with the aid of satellite images of three different years, index methods, and classification approach were compared, it was observed that ISA determined with classification approach yielded better outcomes than the ISA obtained with the NDAISI method. The ISA class (Figs. 3a, 4a, and 5a, white areas) identified with the NDAISI method was mostly confused with soil class.

Accuracy assessment

For ISA classification with SVM, pixels belonging to different sections of the study area were selected on satellite images. For the year 1987, pixels for 2000 ISA and 6500 other areas; for the year 2000, pixels for 2088 ISA and 7030 other areas; for the year 2013, pixels for 2142 ISA and 8148 other areas were selected and classified through training of classification method for each year. For accuracy assessment, 1619 reference points were determined randomly for each satellite image. The land cover type of each reference point was compared with Google Earth satellite images (Estoque et al., 2012; Estoque & Murayama, 2015). Accuracy assessments for SVM

classification result in cases with and without NDAISI data as a supplementary attribute are provided in Table 2. Present findings for 3 years revealed that the use of NDAISI data improved the success of classification.

Because of SVM with NDAISI’s higher accuracy in this study, the method was selected for further analysis in this study. In addition to the overall accuracy and kappa values in Table 2, accuracy assessment was also done based on the producer’s and user’s accuracies in Table 3.

The producer’s accuracy is calculated by proportioning correctly classified pixels of a class to the total pixels appointed to that class in the reference data. User’s accuracy is calculated by proportioning correctly classified pixels of a class to the total pixels appointed to that class in the classified image. The producer’s accuracy measures the success of the classification method. The user’s accuracy measures confidence in the thematic information produced (Sunar et al., 2011). Considering the producer’s accuracies for different years (1987, 2000, and 2013), it was seen that the impervious surface areas were, respectively, classified with lower accuracy (74%, 82%, and 90% for IS class) than other areas (100%, 97%, and 97% for other class). This is due to the similar pixel reflection characteristics of the IS and soil areas (Deng et al., 2015). The user’s accuracies for the IS class (95–100%) were more than the other class (87–95%). This is because there is only one class type in the IS class and more than one class type in the other class. It was seen that sufficient accuracy (above mentioned) was obtained for two classes considering both the producer’s and user’s accuracies.

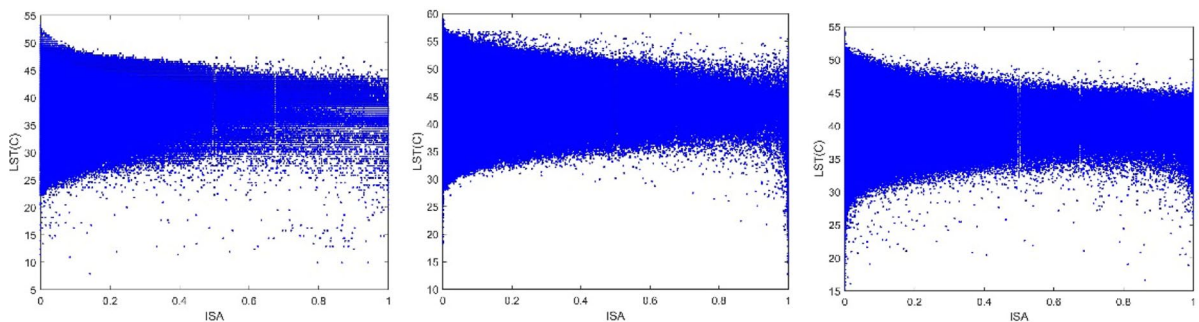


Fig. 6 ISA-LST scatter graphs, respectively, for 1987, 2000, 2013

Determination of ISA-LST relationship

Classifier rule values for ISA class obtained through classification are in the range of 0–1. The values approaching 1 indicate the increasing possibility of a pixel to be an ISA. For a pixel to be classified as ISA, the ISA rule value should be greater than 0.5. In this study, for analysis of the relationships between LST and ISA, the ISA rule and LST values of each pixel were taken into consideration. The ISA-LST scatter graphs of three different years are presented in Fig. 6.

It is important to determine which regression model can be used for each dependent variable. Therefore, drawing the data scatter graphs is necessary. If the data look like a known mathematical function, they can be adapted to the model type. Besides, an experience-based model can also be used (Alexopoulos, 2010). Since the linear regression model was commonly used in literature to model the relationships of ISA, vegetation, and soil classes with LST (Lu & Weng, 2006; Yuan & Bauer, 2007; Imhoff et al., 2010; Rhee et al., 2014), it was preferred also

Fig. 7 ISA-LST relationship graphs during 1987–2013: outcomes of density-based zonal analysis (a, c, e) and pixel-based analysis (b, d, f)

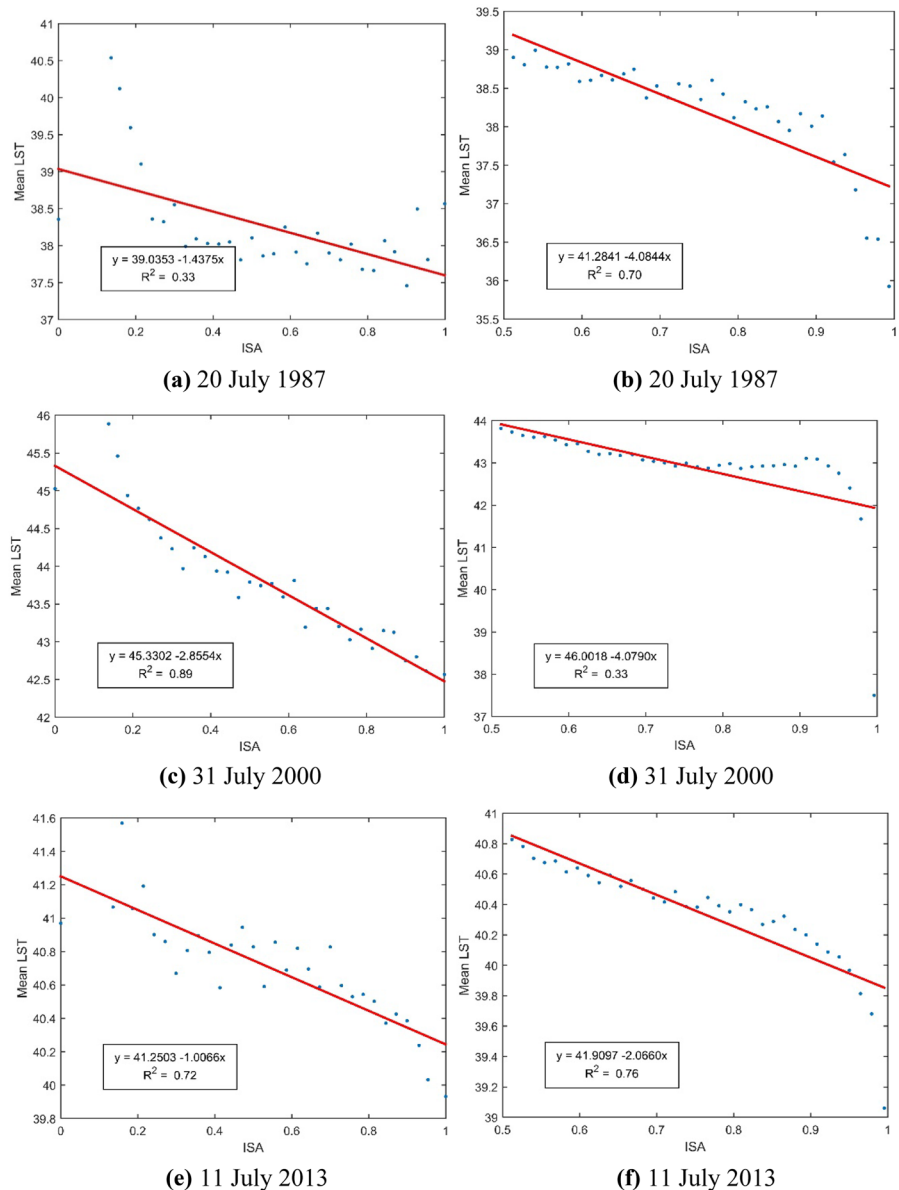
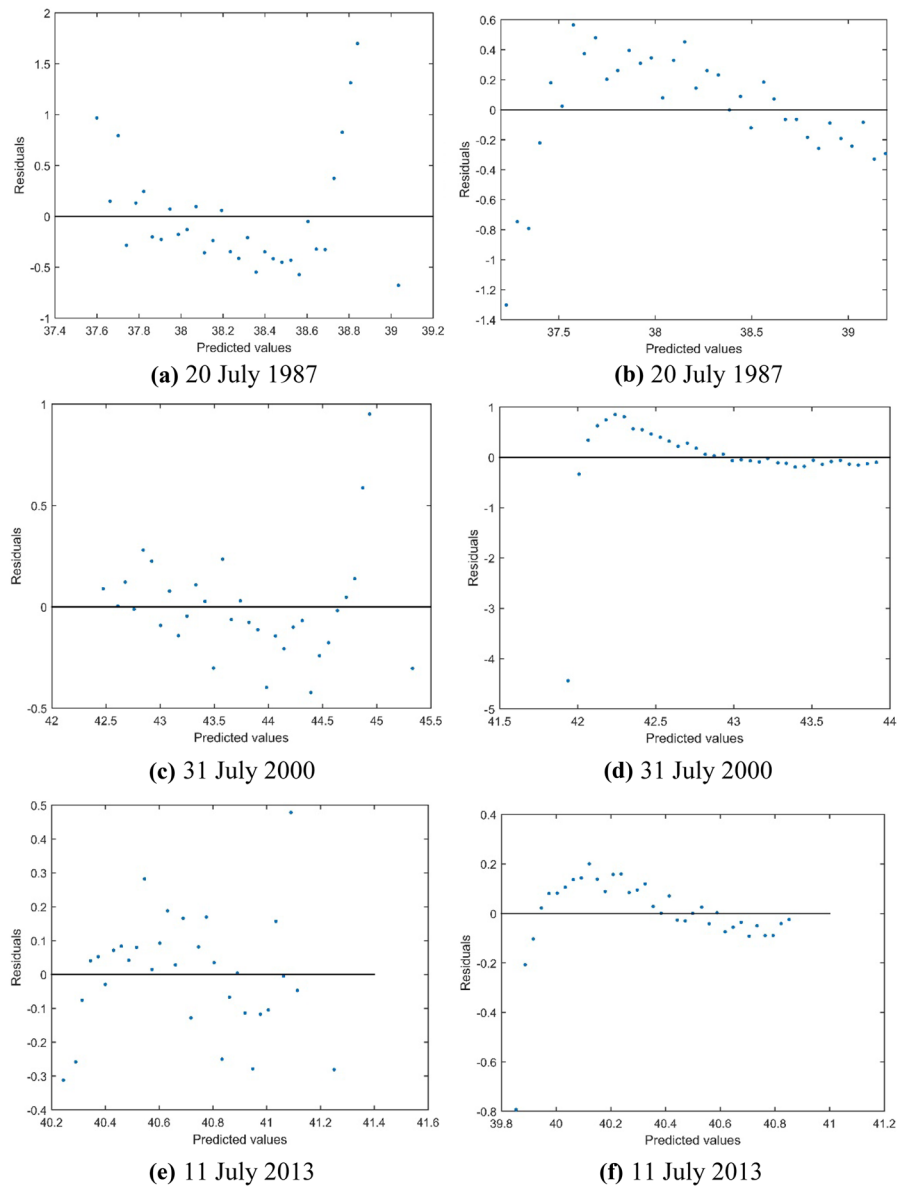


Fig. 8 ISA-LST error graphs during 1987–2013: outcomes of density-based zonal analysis (a, c, e) and pixel-based analysis (b, d, f)



in this study. Different from most of the previous studies, the statistical tests (residual plot, *t*, and *F* tests) conducted for all regression models of the regression analysis were presented in the main text of the paper.

At 0.05 significance level, according to the graph presenting the relationship between ISA-LST, $R^2=0.33$ and $RMSE=0.57$ in DBZA graph (Fig. 7a) and $R^2=0.70$ and $RMSE=0.39$ in PBA graph (Fig. 7b) of 1987; $R^2=0.89$ and $RMSE=0.27$ in DBZA graph (Fig. 7c) and $R^2=0.33$ and

$RMSE=0.85$ in PBA graph (Fig. 7d) of 2000; $R^2=0.72$ and $RMSE=0.18$ in DBZA graph (Fig. 7e) and $R^2=0.76$ and $RMSE=0.17$ in PBA graph (Fig. 7f) of 2013.

To test the validity of the linear model, error scatter graphs, and hypothesis tests (*t* and *F* test) can be used. In the present case, despite the low R^2 values, the linear regression model generated with DBZA (Fig. 7a) was found to be statistically acceptable (Fig. 8a). In literature (Xu, 2010; Xu et al., 2013), the pixel-based approach with a high

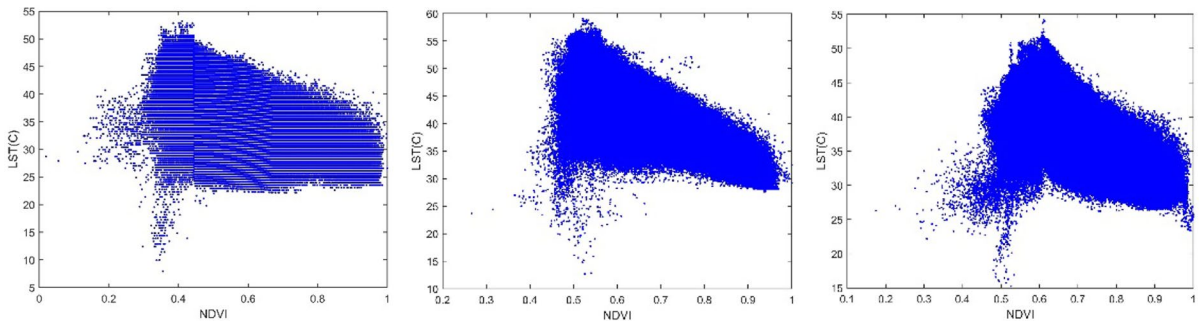


Fig. 9 NDVI-LST scatter graphs, respectively, for 1987, 2000, and 2013

R^2 value was common. However, a certain pattern of error graphs generated with PBA (Fig. 8b, d, f) indicates that the linear regression model was not statistically reliable, because errors are interdependent and not homoscedastic. Such a case was mostly attributed not to take place information, a hidden variable (confounding), into account in the pixel-based approach. The greater significance of DBZA, reflecting place-based neighborhood relationship, supports that idea.

Since it was found to be significant, hypothesis tests were conducted only for DBZAs. The t test was conducted for ISA-LST regression model parameters and the F test was conducted to check the overall significance of the model. Present tests revealed that ISA-LST linear regression model and model parameters were significant. Regression analysis between ISA-LST of the years 1987, 2000, and 2013 yielded a reverse (negative) relationship, in other words, mean LST decreased with increasing possibility of being an ISA.

Determination of NDVI-LST relationship

The values for resultant vegetation index (NDVI) areas were within -1 and 1 interval. NDVI index values approaching 1 express the increasing potential of the pixel of being vegetation. In the present study, vegetation index data of -1 and 1 range was normalized into $0-1$ range, and scatter graphs were generated for 1987, 2000, and 2013 data by taking the vegetation ratios of each pixel ($0-100\%$) into consideration (Xu et al., 2013). NDVI-LST scatter graphs of 3 years are presented in Fig. 9.

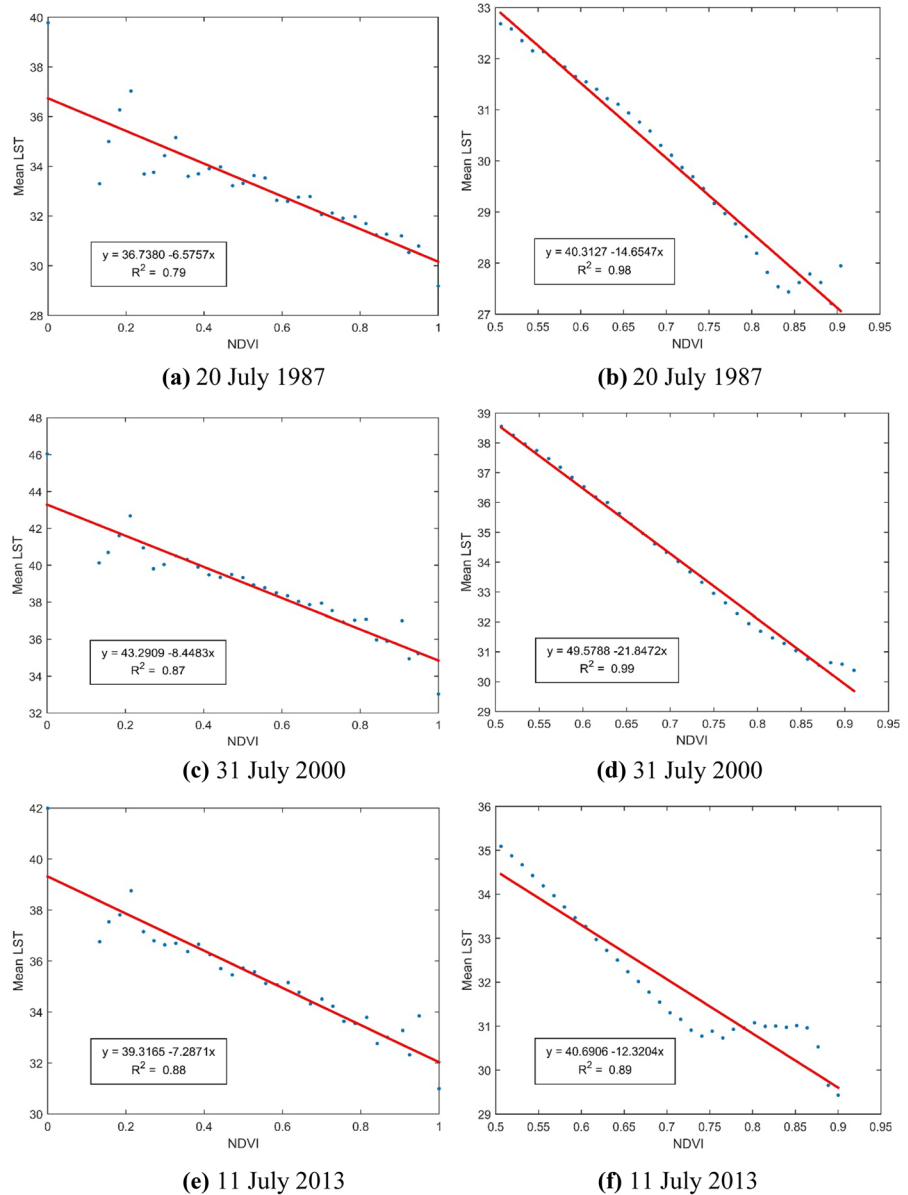
In previous literatures, the places with an NDVI value of greater than 0.5 were accepted as vegetation (Carlson & Ripley, 1997; Sobrino et al., 2004, 2008). Therefore, to present the relationship between vegetation and LST, the pixels with a NDVI value of greater than 0.5 were taken into consideration. At 0.05 significance level, according to the graph presenting the relationship between NDVI-LST, $R^2=0.79$ and $RMSE=0.95$ in DBZA graph (Fig. 10a) and $R^2=0.98$ and $RMSE=0.28$ in PBA graph (Fig. 10b) of 1987; $R^2=0.87$ and $RMSE=0.89$ in DBZA graph (Fig. 10c) and, $R^2=0.99$ and $RMSE=0.25$ in PBA graph (Fig. 10d) of 2000; $R^2=0.88$ and $RMSE=0.74$ in DBZA graph (Fig. 10e) and $R^2=0.89$ and $RMSE=0.52$ in PBA graph (Figs. 10f and 11) of 2013.

Since it was found to be significant (Fig. 11), hypothesis tests were conducted only for the NDVI-LST regression model and model parameters generated with DBZAs. Present F and t tests revealed that model and model parameters were significant. NDVI-LST analyses of 3 years revealed decreasing LST with increasing NDVI values. Such a finding complies with the results of previous studies (Lu & Weng, 2006; Yuan & Bauer, 2007; Zhang et al., 2009; Onishi et al., 2010; Solangi et al., 2019).

Determination of soil-LST relationship

Soil areas were obtained from NDVI data. For NDVI-based soil classes, the pixels with index values of between 0 and 0.2 were taken into consideration (Carlson & Ripley, 1997; Sobrino et al., 2004, 2008). Because of difficulty in distinguishing soil and ISA, the pixels previously decided as ISA based on the

Fig. 10 NDVI-LST relationship graphs during 1987–2013: outcomes of density-based zonal analysis (a, c, e) and pixel-based analysis (b, d, f)

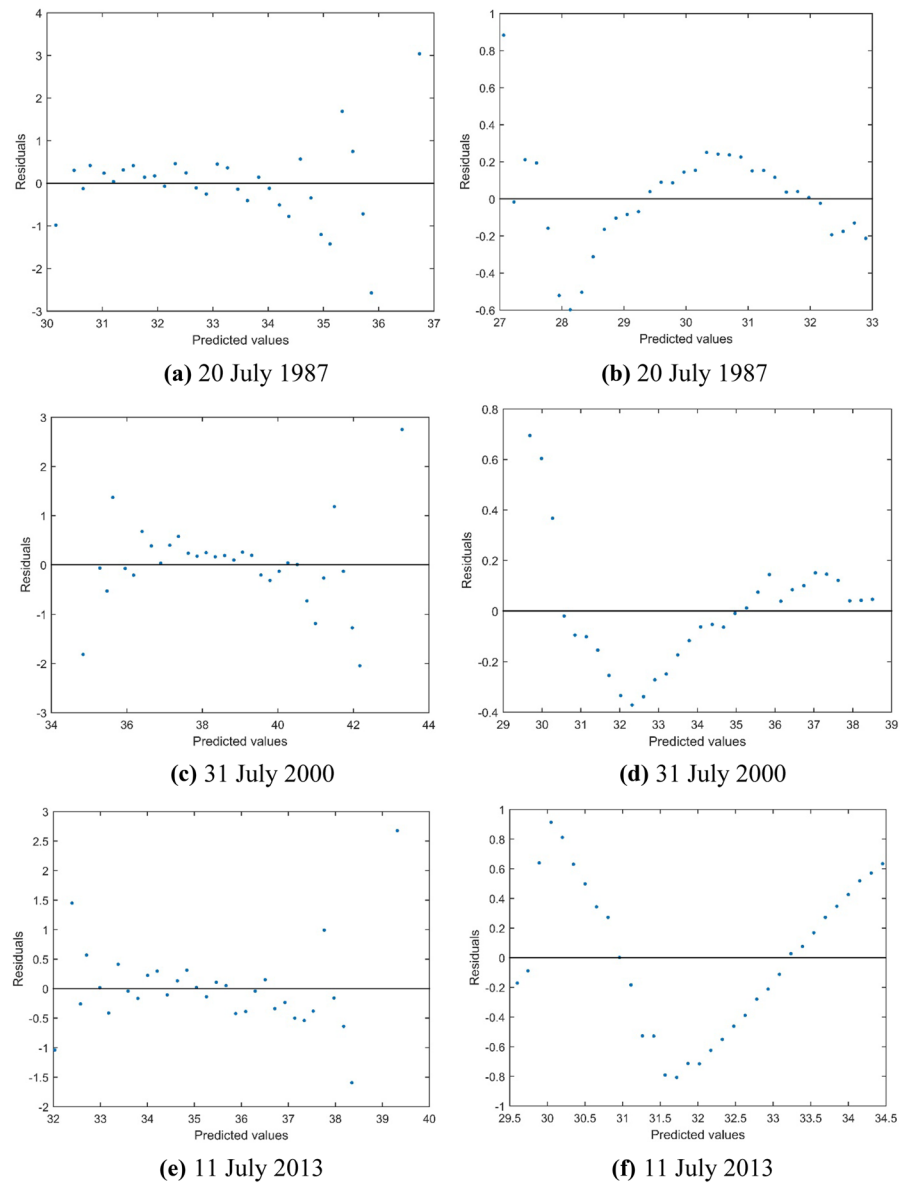


SVM classification method were removed from the soil class. In this way, soil class was identified more reliably.

NDVI and LST values were taken into consideration to determine the soil-LST relationship. To improve comprehension of these values, they were normalized into 0–1 range and the soil ratio of each pixel (0–100%) was determined (Xu et al., 2013). Soil-LST scatter graphs of three different years are presented in Fig. 12.

At 0.05 significance level, according to the graph presenting the relationship between soil-LST, $R^2=0.86$ and $RMSE=0.77$ in DBZA graph (Fig. 13a) and $R^2=0.38$ and $RMSE=0.44$ in PBA graph (Fig. 13b) of 1987; $R^2=0.81$ and $RMSE=1.02$ in DBZA graph (Fig. 13c) and $R^2=0.42$ and $RMSE=1.68$ in PBA graph (Fig. 13d) of 2000; $R^2=0.89$ and $RMSE=0.73$ in DBZA graph (Fig. 13e) and $R^2=0.57$ and $RMSE=2.11$ in PBA graph (Fig. 13f) of 2013.

Fig. 11 NDVI-LST error graphs during 1987–2013: outcomes of density-based zonal analysis (**a, c, e**) and pixel-based analysis (**b, d, f**)



Since it was found to be significant (Fig. 14), hypothesis tests were conducted only for the Soil-LST regression model and model parameters generated with DBZAs. Present F and t tests revealed that model and model parameters were significant. Soil-LST analyses of 3 years revealed increasing LST with increasing soil values (Fig. 14).

In this study, Landsat 5, 7, and 8 satellite images for July of 1987, 2000, and 2013 were used and the relationships of IS, vegetation, and soil areas with LST were investigated and tested statistically. Present analyses revealed that

- Average LST decreased with increasing ISA,
- Average LST decreased with increasing vegetation,
- Average LST increased with increasing soil.

Climate, land cover, and remote sensing satellite systems played a distinctive role in these results. It was observed that the present study area (Fig. 1) was mostly composed of different types of soil areas, quite slightly of water, and slightly of vegetation areas. The present study area, Kayseri province, is a semi-arid region (Erinc, 1950; Helburn, 1955). Semi-arid regions generally have dry soil type and drought

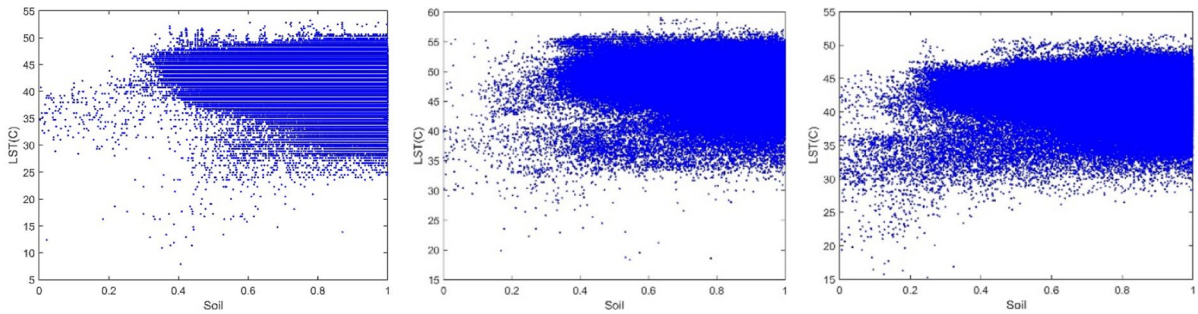


Fig. 12 Soil-LST scatter graphs, respectively, for 1987, 2000, 2013

index (ratio of annual total precipitation to potential evapotranspiration) values of between 0.20 and 0.50 (Lal, 2004; Garcia-Franco et al., 2018). Soils of semi-arid regions are commonly degraded through various land use. Such a case generally ends up with low organic carbon content. Erosion through anthropogenic activities, salinity, and degradation also exert serious threats on soils of semi-arid regions. With these processes, a loss is generated in the water storage of the soils (Garcia-Franco et al., 2018). Reduced soil moisture contents also reduce evaporation, thus increase soil temperature. For a better understanding of such a case, a satellite image of 2013 was used, and a spectral reflectance profile was generated with the aid of atmospherically corrected reflectance values of vegetation, IS, and soil areas (Fig. 15).

In the visible region of Fig. 15 (R: Band 4, G: Band 3, B: Band 2), soil areas had lower reflectance than ISAs, in other words, absorbed more solar energy. Additionally, soil areas have greater emissivity values than ISAs (Wang et al., 2015a). Then, soil areas are hotter than ISAs. ISAs reflecting solar energy more and thus were cooler than soil areas. The case is somehow different in vegetation areas. Vegetation uses the energy absorbed in the visible region for photosynthesis (Sunar et al., 2011). Therefore, vegetation areas do not get hot as much as IS and soil areas.

In LST analyses made with satellite images, seasonal conditions at the time of imaging and albedo of the materials are quite effective (Yılmaz, 2015). Such a case is also related to specific heat, thermal

diffusion, and conductance of concrete, asphalt, and tile-like materials used in buildings constructed in ISAs. Since ISAs have high specific heat values, ISAs are heated more slowly than soil areas despite the same quantity of incoming solar energy to different vegetation types.

Present findings on ISA-LST and Soil-LST relationships were contradictory with some earlier studies (Lu & Weng, 2006; Yuan & Bauer, 2007; Onishi et al., 2010), but supporting or parallel with some others (Çiçek et al., 2013; Yılmaz, 2015; Haashemi et al., 2016; Wei & Blaschke, 2018). Yılmaz (2015) used Landsat images of summer months and reported greater LST values for dry farming lands (soil) than for urban areas. Wei and Blaschke (2018) conducted a study in Guangzhou, a rapidly growing province of China, and reported that the majority of high LST values belonged to places with low ISA values. Haashemi et al. (2016) reported that in day-time satellite image data (Landsat 8), the temperature of soil areas was greater than the temperatures of IS, vegetation, and water areas throughout the year. However, in night data (MODIS), greater temperatures were reported for ISAs than for soil areas. Çiçek et al. (2013) reported seasonal differences in characteristics of heat island obtained from Landsat images of Ankara province and such a difference varied based on the time of the day. It was reported that at the time of satellite imaging (10.00 o'clock), there was a negative heat island impact in all months of the year; in other words, soil areas were hotter than urban areas.

Fig. 13 Soil-LST relationship graphs during 1987–2013: outcomes of density-based zonal analysis (a, c, e) and pixel-based analysis (b, d, f)

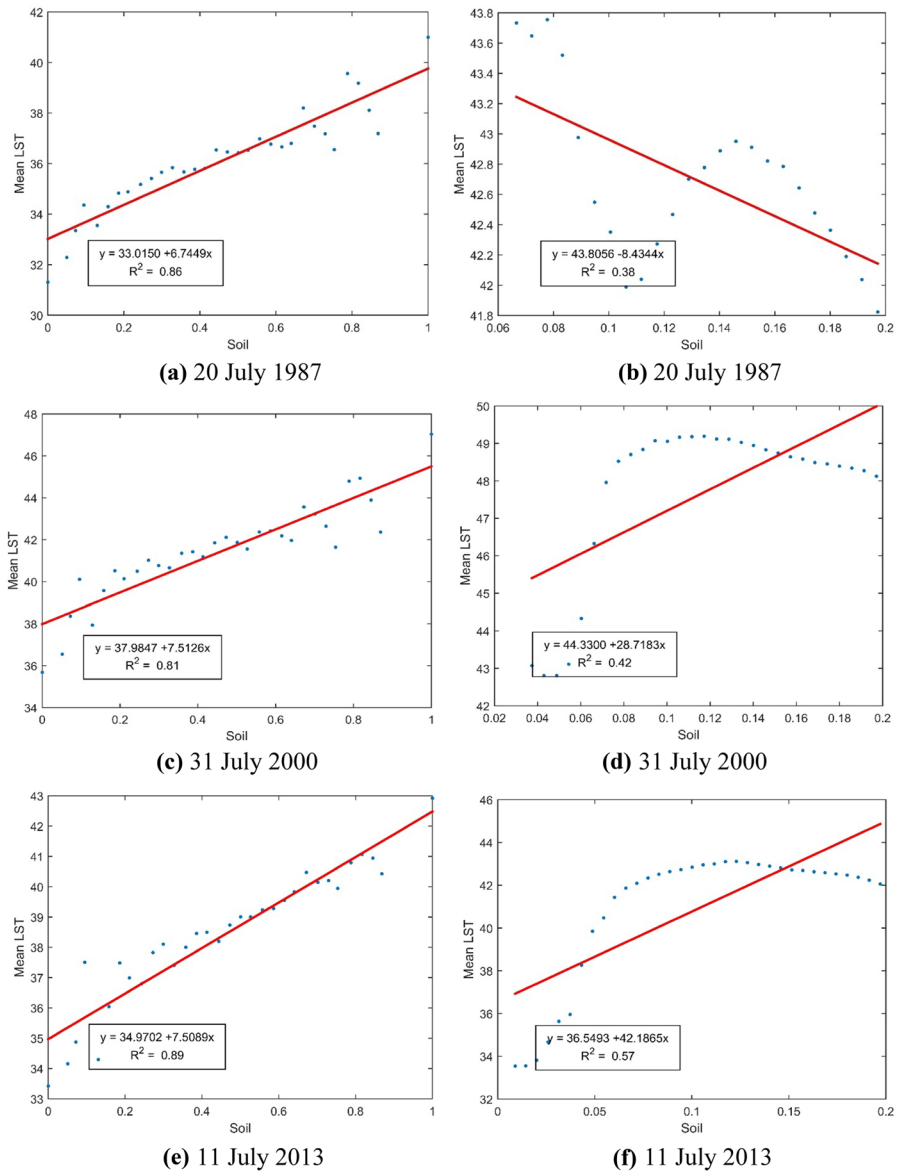


Fig. 14 Soil-LST error graphs during 1987–2013: outcomes of density-based zonal analysis (**a, c, e**) and pixel-based analysis (**b, d, f**)

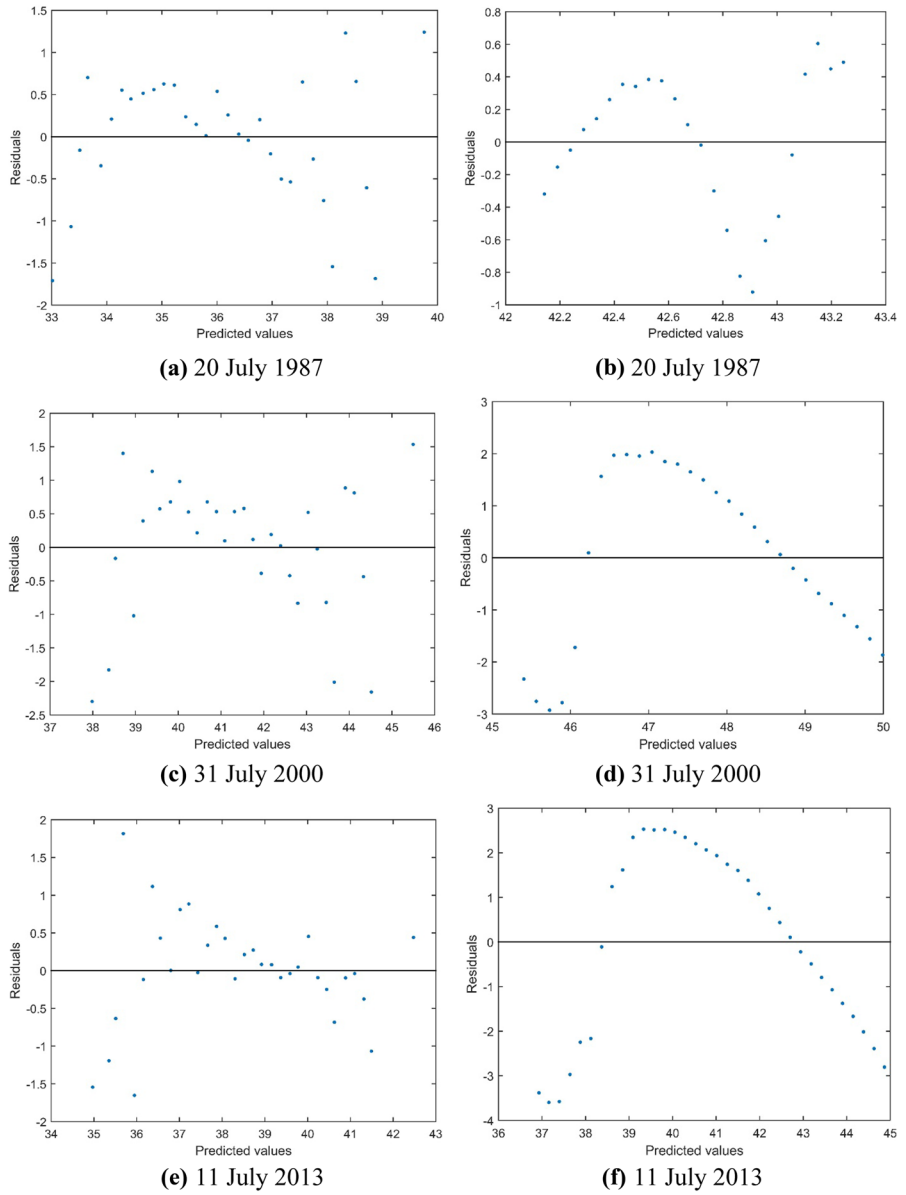
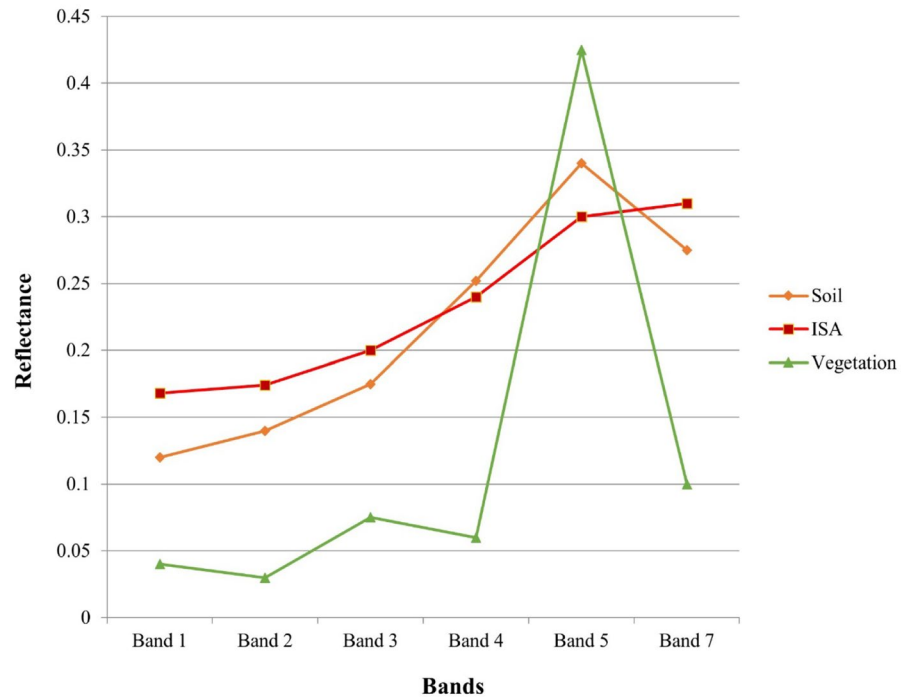


Fig. 15 Spectral reflectance profile for vegetation (green), IS (red), and soil (brown) of 2013 data



Conclusion

This study was conducted to analyze the relationships of impervious surface, vegetation, and soil areas with land surface temperatures in urban and rural sections of Kayseri province with a semi-arid climate. Initially, impervious surfaces were determined with the aid of the SVM supervised classification method; then, the other classes were determined with the use of NDVI data and impervious surface class information. It was observed that NDAISI data improved SVM classification results (overall accuracies $\geq 90.30\%$ and kappa $\geq 78.20\%$) in the detection of impervious surfaces hard to distinguish from the soil. In the practice of SVM, visible, near-infrared, short wave infrared, and thermal region bands of satellite images in attribute space and NDAISI data were used. It was observed in this study that NDAISI data were not efficient alone in the detection of impervious surfaces. The relationships between land cover classes and land surface temperatures were analyzed with the aid of simple linear regression models. To generate input and output data required for regression models to be set up, besides common pixel-based and classical regional-based approaches, a specific DBZA approach was developed in this study. It was observed that this

original approach yielded better statistical outcomes than the other approaches. Strong negative linear relationships between NDVI and mean land surface temperatures were demonstrated with R^2 more than 0.8. ISAs and soil areas of the present study area had inverse relationships with land surface temperatures. In other words, mean land surface temperatures decreased with increasing ISAs ($R^2=0.33$, $R^2=0.89$, and $R^2=0.72$) and increased with increasing soil surface areas ($R^2=0.86$, $R^2=0.81$, and $R^2=0.89$), respectively, for 1987, 2000, and 2013. Such findings were attributed to the climate and land cover of the study area. The present study area has a semi-arid climate. In semi-arid regions, quite low soil moisture levels reduce thermal capacity and heat conductance of soils, then soil areas are heated more rapidly than the ISAs complying with sensing time of satellite images (10:00 am local mean time). Besides, in semi-arid regions, newly constructed impervious surfaces reduce mean land surface temperatures since such areas are mostly constructed over soils with low vegetation. This study presents useful information in terms of the performance of ISA analysis with the use of the SVM classification method with the aid of NDAISI index data for semi-arid regions. The use of a new density-based regional analysis approach

developed in this study can provide better-reflected relationships between two different land cover classes in a future study. Besides, the use of more satellite images with higher spatial resolution such as ASTER satellite and covering different regional areas in different climatic zones is suggested to enhance the quantitative assessment of impervious surfaces. Thus, it can be possible to better detect the impacts of urbanization on thermal environments.

Funding This work was supported by the Scientific and Technological Research Council of Turkey under 2211-C priority areas Ph.D. scholarship.

Declarations

Conflict of interest The authors declare that they have no conflict of interest.

References

Acero, J. A., & González-Asensio, B. (2018). Influence of vegetation on the morning land surface temperature in a tropical humid urban area. *Urban Climate*, 26, 231–243. <https://doi.org/10.1016/j.uclim.2018.09.004>.

Alexopoulos, E. C. (2010). Introduction to multivariate regression analysis. *Hippokratia*, 14(1), 23–28.

Arnold, C. L., Jr., & Gibbons, C. J. (1996). Impervious surface coverage: the emergence of a key environmental indicator. *Journal of the American Planning Association*, 62(2), 243–258. <https://doi.org/10.1080/01944369608975688>.

Bauer, M. E., Heinert, N. J., Doyle, J. K., & Yuan, F. (2004). Impervious surface mapping and change monitoring using Landsat remote sensing. In *ASPRS Annual Conference Proceedings* : American Society for Photogrammetry and Remote Sensing Bethesda, MD, (Vol. 10)

Bhatti, N. B., Siyal, A. A., Qureshi, A. L., & Bhatti, I. A. (2019). Land covers change assessment after small dam’s construction based on the satellite data. *Civil Engineering Journal*, 5(4), 810–818. <https://doi.org/10.28991/cej-2019-03091290>.

Bierwagen, B. G., Theobald, D. M., Pyke, C. R., Choate, A., Groth, P., Thomas, J. V., et al. (2010). National housing and impervious surface scenarios for integrated climate impact assessments. *Proceedings of the National Academy of Sciences*, 107(49), 20887–20892. <https://doi.org/10.1073/pnas.1002096107>.

Carlson, T. N., & Ripley, D. A. (1997). On the relation between NDVI, fractional vegetation cover, and leaf area index. *Remote Sensing of Environment*, 62(3), 241–252. [https://doi.org/10.1016/S0034-4257\(97\)00104-1](https://doi.org/10.1016/S0034-4257(97)00104-1).

Chander, G., & Markham, B. (2003). Revised Landsat-5 TM radiometric calibration procedures and postcalibration dynamic ranges. *IEEE Transactions on Geoscience and Remote Sensing*, 41(11), 2674–2677. <https://doi.org/10.1109/TGRS.2003.818464>.

Couturier, S., Ricárdez, M., Osorno, J., & López-Martínez, R. (2011). Morpho-spatial extraction of urban nuclei in diffusely urbanized metropolitan areas. *Landscape and Urban Planning*, 101(4), 338–348. <https://doi.org/10.1016/j.landurbplan.2011.02.039>.

Çiçek, İ, Yılmaz, E., Türkoğlu, N., & Çalıřkan, O. (2013). Seasonal variation of surface temperature based on land cover in Ankara. *Journal of Human Sciences*, 10(1), 621–640.

Deng, C., & Wu, C. (2012). BCI: A biophysical composition index for remote sensing of urban environments. *Remote Sensing of Environment*, 127, 247–259. <https://doi.org/10.1016/j.rse.2012.09.009>.

Deng, Y., Wu, C., Li, M., & Chen, R. (2015). RNDSI: A ratio normalized difference soil index for remote sensing of urban/suburban environments. *International Journal of Applied Earth Observation and Geoinformation*, 39, 40–48. <https://doi.org/10.1016/j.jag.2015.02.010>.

Du, Z., Li, W., Zhou, D., Tian, L., Ling, F., Wang, H., et al. (2014). Analysis of Landsat-8 OLI imagery for land surface water mapping. *Remote Sensing Letters*, 5(7), 672–681. <https://doi.org/10.1080/2150704X.2014.960606>.

Erinc, S. (1950). Climatic types and the variation of moisture regions in Turkey. *Geographical Review*, 40(2), 224–235. <https://doi.org/10.2307/211281>.

Esch, T., Himmler, V., Schorcht, G., Thiel, M., Wehrmann, T., Bachofer, F., et al. (2009). Large-area assessment of impervious surface based on integrated analysis of single-date Landsat-7 images and geospatial vector data. *Remote Sensing of Environment*, 113(8), 1678–1690. <https://doi.org/10.1016/j.rse.2009.03.012>.

Estoque, R. C., Estoque, R. S., & Murayama, Y. (2012). Prioritizing areas for rehabilitation by monitoring change in barangay-based vegetation cover. *ISPRS International Journal of Geo-Information*, 1(1), 46–68. <https://doi.org/10.3390/ijgi1010046>.

Estoque, R. C., & Murayama, Y. (2015). Classification and change detection of built-up lands from Landsat-7 ETM+ and Landsat-8 OLI/TIRS imageries: A comparative assessment of various spectral indices. *Ecological Indicators*, 56, 205–217. <https://doi.org/10.1016/j.ecolind.2015.03.037>.

Estoque, R. C., Murayama, Y., & Myint, S. W. (2017). Effects of landscape composition and pattern on land surface temperature: An urban heat island study in the megacities of Southeast Asia. *Science of the Total Environment*, 577, 349–359. <https://doi.org/10.1016/j.scitotenv.2016.10.195>.

Garcia-Franco, N., Hobley, E., Hübner, R., & Wiesmeier, M. (2018). Climate-smart soil management in semiarid regions. In *Soil Management and Climate Change* (pp. 349–368): Elsevier.

Gluch, R., Quattrochi, D. A., & Luvall, J. C. (2006). A multi-scale approach to urban thermal analysis. *Remote Sensing of Environment*, 104(2), 123–132. <https://doi.org/10.1016/j.rse.2006.01.025>.

Govil, H., Guha, S., Dey, A., & Gill, N. (2019). Seasonal evaluation of downscaled land surface temperature: A case study in a humid tropical city. *Heliyon*, 5(6), e01923. <https://doi.org/10.1016/j.heliyon.2019.e01923>.

Guan, X., Shen, H., Li, X., Gan, W., & Zhang, L. (2019). A long-term and comprehensive assessment of the urbanization-induced impacts on vegetation net primary productivity.

- Science of The Total Environment*, 669, 342–352. <https://doi.org/10.1016/j.scitotenv.2019.02.361>.
- Haashemi, S., Weng, Q., Darvishi, A., & Alavipanah, S. K. (2016). Seasonal variations of the surface urban heat island in a semi-arid city. *Remote Sensing*, 8(4), 352. <https://doi.org/10.3390/rs8040352>.
- Helburn, N. (1955). A stereotype of agriculture in semiarid Turkey. *Geographical Review*, 45(3), 375–384. <https://doi.org/10.2307/211810>.
- Imhoff, M. L., Zhang, P., Wolfe, R. E., & Bounoua, L. (2010). Remote sensing of the urban heat island effect across biomes in the continental USA. *Remote Sensing of Environment*, 114(3), 504–513. <https://doi.org/10.1016/j.rse.2009.10.008>.
- Jennings, D. B., Jarnagin, S. T., & Ebert, D. W. (2004). A modeling approach for estimating watershed impervious surface area from National Land Cover Data 92. *Photogrammetric Engineering & Remote Sensing*, 70(11), 1295–1307. <https://doi.org/10.14358/PERS.70.11.1295>.
- Kalnay, E., & Cai, M. (2003). Impact of urbanization and land-use change on climate. *Nature*, 423(6939), 528–531. <https://doi.org/10.1038/nature01675>.
- Kaufmann, R. K., Seto, K. C., Schneider, A., Liu, Z., Zhou, L., & Wang, W. (2007). Climate response to rapid urban growth: Evidence of a human-induced precipitation deficit. *Journal of Climate*, 20(10), 2299–2306. <https://doi.org/10.1175/JCLI4109.1>.
- Kesikoglu, M. H., Atasever, U. H., Dadaser-Celik, F., & Ozkan, C. (2019). Performance of ANN, SVM and MLH techniques for land use/cover change detection at Sultan Marshes wetland. *Turkey. Water Science and Technology*, 80(3), 466–477. <https://doi.org/10.2166/wst.2019.290>.
- Kesikoğlu, M. H. (2013). *Sultan sazlığı milli parkı ve Ramsar alanı kıyı değişiminin uydu görüntü analizleriyle incelenmesi*. MSc thesis, Erciyes University, Kayseri, Turkey.
- Lal, R. (2004). Carbon sequestration in dryland ecosystems. *Environmental Management*, 33(4), 528–544. <https://doi.org/10.1007/s00267-003-9110-9>.
- Li, J., Song, C., Cao, L., Zhu, F., Meng, X., & Wu, J. (2011). Impacts of landscape structure on surface urban heat islands: A case study of Shanghai. *China. Remote Sensing of Environment*, 115(12), 3249–3263. <https://doi.org/10.1016/j.rse.2011.07.008>.
- Li, P., Jiang, L., & Feng, Z. (2014). Cross-comparison of vegetation indices derived from Landsat-7 enhanced thematic mapper plus (ETM+) and Landsat-8 operational land imager (OLI) sensors. *Remote Sensing*, 6(1), 310–329. <https://doi.org/10.3390/rs6010310>.
- Li, W., Du, Z., Ling, F., Zhou, D., Wang, H., Gui, Y., et al. (2013). A comparison of land surface water mapping using the normalized difference water index from TM, ETM+ and ALI. *Remote Sensing*, 5(11), 5530–5549. <https://doi.org/10.3390/rs5115530>.
- Lu, D., & Weng, Q. (2006). Spectral mixture analysis of ASTER images for examining the relationship between urban thermal features and biophysical descriptors in Indianapolis, Indiana, USA. *Remote Sensing of Environment*, 104(2), 157–167. <https://doi.org/10.1016/j.rse.2005.11.015>.
- Lyu, R., Clarke, K. C., Zhang, J., Jia, X., Feng, J., & Li, J. (2019). The impact of urbanization and climate change on ecosystem services: A case study of the city belt along the Yellow River in Ningxia, China. *Computers, Environment and Urban Systems*, 77, 101351. <https://doi.org/10.1016/j.compenvurb.2019.101351>.
- Ma, T., Zhou, C., Pei, T., Haynie, S., & Fan, J. (2012). Quantitative estimation of urbanization dynamics using time series of DMSP/OLS nighttime light data: A comparative case study from China's cities. *Remote Sensing of Environment*, 124, 99–107. <https://doi.org/10.1016/j.rse.2012.04.018>.
- Nichol, J. (2005). Remote sensing of urban heat islands by day and night. *Photogrammetric Engineering & Remote Sensing*, 71(5), 613–621. <https://doi.org/10.14358/PERS.71.5.613>.
- Okujeni, A., van der Linden, S., & Hostert, P. (2015). Extending the vegetation-impervious-soil model using simulated EnMAP data and machine learning. *Remote Sensing of Environment*, 158, 69–80. <https://doi.org/10.1016/j.rse.2014.11.009>.
- Onishi, A., Cao, X., Ito, T., Shi, F., & Imura, H. (2010). Evaluating the potential for urban heat-island mitigation by greening parking lots. *Urban Forestry & Urban Greening*, 9(4), 323–332. <https://doi.org/10.1016/j.ufug.2010.06.002>.
- Otsu, N. (1979). A threshold selection method from gray-level histograms. *IEEE Transactions on Systems, Man and Cybernetics*, 9(1), 62–66. <https://doi.org/10.1109/TSMC.1979.4310076>.
- Paul, M. J., & Meyer, J. L. (2001). Streams in the urban landscape. *Annual Review of Ecology and Systematics*, 32(1), 333–365. <https://doi.org/10.1146/annurev.ecolsys.32.081501.114040>.
- Phinn, S., Stanford, M., Scarth, P., Murray, A., & Shyy, P. (2002). Monitoring the composition of urban environments based on the vegetation-impervious surface-soil (VIS) model by subpixel analysis techniques. *International Journal of Remote Sensing*, 23(20), 4131–4153. <https://doi.org/10.1080/01431160110114998>.
- Piyooosh, A. K., & Ghosh, S. K. (2017). Semi-automatic mapping of anthropogenic impervious surfaces in an urban/suburban area using Landsat 8 satellite data. *GIScience & Remote Sensing*, 54(4), 471–494. <https://doi.org/10.1080/15481603.2017.1282414>.
- Piyooosh, A. K., & Ghosh, S. K. (2018). Development of a modified bare soil and urban index for Landsat 8 satellite data. *Geocarto International*, 33(4), 423–442. <https://doi.org/10.1080/10106049.2016.1273401>.
- Rashid, I., & Romshoo, S. A. (2013). Impact of anthropogenic activities on water quality of Lidder River in Kashmir Himalayas. *Environmental Monitoring and Assessment*, 185(6), 4705–4719. <https://doi.org/10.1007/s10661-012-2898-0>.
- Rhee, J., Park, S., & Lu, Z. (2014). Relationship between land cover patterns and surface temperature in urban areas. *GIScience & Remote Sensing*, 51(5), 521–536. <https://doi.org/10.1080/15481603.2014.964455>.
- Sahu, S., Prasad, M., & Tripathy, B. (2015). A support vector machine binary classification and image segmentation of remote sensing data of Chilika Lagoon. *IJRIT International Journal of Research in Information Technology*, 3(5), 191–204.
- Sekertekin, A., Kutoglu, S. H., & Kaya, S. (2016). Evaluation of spatio-temporal variability in land surface temperature: A case study of Zonguldak. *Turkey. Environmental Monitoring and Assessment*, 188(1), 30. <https://doi.org/10.1007/s10661-015-5032-2>.

- Sobrino, J. A., Jiménez-Muñoz, J. C., & Paolini, L. (2004). Land surface temperature retrieval from Landsat TM 5. *Remote Sensing of Environment*, 90(4), 434–440. <https://doi.org/10.1016/j.rse.2004.02.003>.
- Sobrino, J. A., Jiménez-Muñoz, J. C., Sòria, G., Romaguera, M., Guanter, L., Moreno, J., et al. (2008). Land surface emissivity retrieval from different VNIR and TIR sensors. *IEEE Transactions on Geoscience and Remote Sensing*, 46(2), 316–327. <https://doi.org/10.1109/TGRS.2007.904834>.
- Solangi, G. S., Siyal, A. A., & Siyal, P. (2019). Spatiotemporal dynamics of land surface temperature and its impact on the vegetation. *Civil Engineering Journal*, 5(8), 1753–1763. <https://doi.org/10.28991/cej-2019-03091368>.
- Sun, Y., Gao, C., Li, J., Wang, R., & Liu, J. (2019). Quantifying the effects of urban form on land surface temperature in subtropical high-density urban areas using machine learning. *Remote Sensing*, 11(8), 959. <https://doi.org/10.3390/rs11080959>.
- Sunar, F., Özkan, C., & Osmanoglu, B. (2011). *Uzaktan Algılama* (1st ed.). Eskişehir, Turkey: Anadolu Üniversitesi Yayınları.
- UNPD. (2015). World urbanization prospects: the 2014 revision. <https://population.un.org/wup/Publications/Files/WUP2014-Report.pdf>.
- USGS. (2018). Using the USGS Landsat 8 Level 1 Data Product. <https://landsat.usgs.gov/using-usgs-landsat-8-product>.
- Wang, F., Qin, Z., Song, C., Tu, L., Karnieli, A., & Zhao, S. (2015a). An improved mono-window algorithm for land surface temperature retrieval from Landsat 8 thermal infrared sensor data. *Remote Sensing*, 7(4), 4268–4289. <https://doi.org/10.3390/rs70404268>.
- Wang, Z., Gang, C., Li, X., Chen, Y., & Li, J. (2015b). Application of a normalized difference impervious index (NDII) to extract urban impervious surface features based on Landsat TM images. *International Journal of Remote Sensing*, 36(4), 1055–1069. <https://doi.org/10.1080/01431161.2015.1007250>.
- Wei, C., & Blaschke, T. (2018). Pixel-wise vs. object-based impervious surface analysis from remote sensing: correlations with land surface temperature and population density. *Urban Science*, 2(1), 2. <https://doi.org/10.3390/urbansci2010002>.
- Weng, Q., Lu, D., & Schubring, J. (2004). Estimation of land surface temperature–vegetation abundance relationship for urban heat island studies. *Remote Sensing of Environment*, 89(4), 467–483. <https://doi.org/10.1016/j.rse.2003.11.005>.
- Wikipedia (2019). General Information about Kayseri. <https://tr.wikipedia.org/wiki/Kayseri>.
- Wu, C., & Murray, A. T. (2003). Estimating impervious surface distribution by spectral mixture analysis. *Remote Sensing of Environment*, 84(4), 493–505. [https://doi.org/10.1016/S0034-4257\(02\)00136-0](https://doi.org/10.1016/S0034-4257(02)00136-0).
- Xian, G., & Crane, M. (2005). Assessments of urban growth in the Tampa Bay watershed using remote sensing data. *Remote Sensing of Environment*, 97(2), 203–215. <https://doi.org/10.1016/j.rse.2005.04.017>.
- Xian, G., Crane, M., & McMahon, C. (2008). Quantifying multi-temporal urban development characteristics in Las Vegas from Landsat and ASTER data. *Photogrammetric Engineering & Remote Sensing*, 74(4), 473–481. <https://doi.org/10.14358/PERS.74.4.473>.
- Xu, H. (2010). Analysis of impervious surface and its impact on urban heat environment using the normalized difference impervious surface index (NDISI). *Photogrammetric Engineering & Remote Sensing*, 76(5), 557–565. <https://doi.org/10.14358/PERS.76.5.557>.
- Xu, H., Lin, D., & Tang, F. (2013). The impact of impervious surface development on land surface temperature in a subtropical city: Xiamen. *China. International Journal of Climatology*, 33(8), 1873–1883. <https://doi.org/10.1002/joc.3554>.
- Yang, X., & Liu, Z. (2005). Use of satellite-derived landscape imperviousness index to characterize urban spatial growth. *Computers, Environment and Urban Systems*, 29(5), 524–540. <https://doi.org/10.1016/j.compenvurbsys.2005.01.005>.
- Yılmaz, E. (2015). Landsat görüntüleri ile Adana yüzey ısı adası (Adana Surface Heat Island using Landsat Images). *Coğrafi Bilimler Dergisi/Turkish Journal of Geographical Sciences*, 13(2), 115–138.
- Yuan, F., & Bauer, M. E. (2007). Comparison of impervious surface area and normalized difference vegetation index as indicators of surface urban heat island effects in Landsat imagery. *Remote Sensing of Environment*, 106(3), 375–386. <https://doi.org/10.1016/j.rse.2006.09.003>.
- Zhang, Y., Odeh, I. O., & Han, C. (2009). Bi-temporal characterization of land surface temperature in relation to impervious surface area, NDVI and NDBI, using a sub-pixel image analysis. *International Journal of Applied Earth Observation and Geoinformation*, 11(4), 256–264. <https://doi.org/10.1016/j.jag.2009.03.001>.

Publisher's Note Springer Nature remains neutral with regard to jurisdictional claims in published maps and institutional affiliations.